Editors' Suggestion | Featured in Physics

Design of an inertial fusion experiment exceeding the Lawson criterion for ignition

A. L. Kritcher,[1,*] A. B. Zylstra,[1] D. A. Callahan,[1] O. A. Hurricane,[1] C. R. Weber,[1] D. S. Clark,[1] C. V. Young,[1] J. E. Ralph,[1] D. T. Casey,[1] A. Pak,[1] O. L. Landen,[1] B. Bachmann,[1] K. L. Baker,[1] L. Berzak Hopkins,[1] S. D. Bhandarkar,[1] J. Biener,[1] R. M. Bionta,[1] N. W. Birge,[2] T. Braun,[1] T. M. Briggs,[1] P. M. Celliers,[1] H. Chen,[1] C. Choate,[1] L. Divol,[1] T. Döppner,[1] D. Fittinghoff,[1] M. J. Edwards,[1] M. Gatu Johnson,[3] N. Gharibyan,[1] S. Haan,[1] K. D. Hahn,[1] E. Hartouni,[1] D. E. Hinkel,[1] D. D. Ho,[1] M. Hohenberger,[1] J. P. Holder,[1] H. Huang,[4] N. Izumi,[1] J. Jeet,[1] O. Jones,[1] S. M. Kerr,[1] S. F. Khan,[1] H. Geppert Kleinrath,[2] V. Geppert Kleinrath,[2] C. Kong,[4] K. M. Lamb,[2] S. Le Pape,[5] N. C. Lemos,[1] J. D. Lindl,[1] B. J. MacGowan,[1] A. J. Mackinnon,[1] A. G. MacPhee,[1] E. V. Marley,[1] K. Meaney,[2] M. Millot,[1] A. S. Moore,[1] K. Newman,[1] J.-M. G. Di Nicola,[1] A. Nikroo,[1] R. Nora,[1] P. K. Patel,[1,†] N. G. Rice,[4] M. S. Rubery,[1] J. Sater,[1] D. J. Schlossberg,[1] S. M. Sepke,[1] K. Sequoia,[4] S. J. Shin,[1] M. Stadermann,[1] S. Stoupin,[1] D. J. Strozzi,[1] C. A. Thomas,[6] R. Tommasini,[1] C. Trosseille,[1] E. R. Tubman,[1] P. L. Volegov,[2] C. Wild,[7] D. T. Woods,[1] and S. T. Yang[1]

[1]*Lawrence Livermore National Laboratory, P.O. Box 808, Livermore, California 94551-0808, USA*
[2]*Los Alamos National Laboratory, Mail Stop F663, Los Alamos, New Mexico 87545, USA*
[3]*Massachusetts Institute of Technology, Cambridge, Massachusetts 02139, USA*
[4]*General Atomics, San Diego, California 92186, USA*
[5]*Laboratoire pour l'utilisation des Lasers Intenses chez École Polytechnique, F-91128 Palaiseau cedex, France*
[6]*Laboratory for Laser Energetics, University of Rochester, Rochester, New York 14623, USA*
[7]*Diamond Materials Gmbh, 79108 Freiburg, Germany*

(Received 22 June 2022; accepted 13 July 2022; published 8 August 2022)

We present the design of the first igniting fusion plasma in the laboratory by Lawson's criterion that produced 1.37 MJ of fusion energy, Hybrid-E experiment N210808 (August 8, 2021) [Phys. Rev. Lett. **129**, 075001 (2022)]. This design uses the indirect drive inertial confinement fusion approach to heat and compress a central "hot spot" of deuterium-tritium (DT) fuel using a surrounding dense DT fuel piston. Ignition occurs when the heating from absorption of α particles created in the fusion process overcomes the loss mechanisms in the system for a duration of time. This letter describes key design changes which enabled a ~3–6× increase in an ignition figure of merit (generalized Lawson criterion) [Phys. Plasmas **28**, 022704 (2021), Phys. Plasmas **25**, 122704 (2018)]) and an eightfold increase in fusion energy output compared to predecessor experiments. We present simulations of the hot-spot conditions for experiment N210808 that show fundamentally different behavior compared to predecessor experiments and simulated metrics that are consistent with N210808 reaching for the first time in the laboratory "ignition."

DOI: 10.1103/PhysRevE.106.025201

I. INTRODUCTION

Achieving fusion "ignition" in the laboratory has been a long-standing milestone for more than 50 years due to the promise of clean limitless energy and is required for net energy gain in the inertial confinement fusion approach [1,2]. However, the conditions required for this to occur are very difficult to create, more than 50 million degrees to overcome the Coulomb barrier for sufficient deuterium and tritium nuclei to fuse [D + T → n (14.1 MeV)+^{4}He (3.5 MeV)] [3]. Central hot-spot ignition [4] aims to achieve these conditions by compressing and heating a small fraction of the initial deuterium-tritium (DT) fuel ("hot spot") using a higher density DT fuel piston accelerated to high velocities ($v_{\mathrm{imp}} \sim 400$ km/s) that does mechanical work on the hot spot. High areal densities ($> 0.4\,\mathrm{g\,cm^{-2}}$) are also required for absorption of energetic α particles (^{4}He) born in the fusion process and subsequent reheating of the hot-spot plasma. This extra heating by α particles is needed to overcome energy losses in the system, including bremsstrahlung x-ray losses, conduction losses, and explosion losses (or loss of confinement) for a duration of time ("Lawson-like" ignition criteria) [5] for the plasma to "ignite." Until now, reaching the extreme temperature and pressure conditions required for ignition have occurred only in astrophysical plasmas and thermonuclear weapon explosions.

In this work we present design of the first controlled fusion experiment to exceed Lawson-like ignition criteria at the National Ignition Facility (NIF) [8]; see also the accompanying papers which describe the experimental results [9]

*kritcher2@llnl.gov
†Now at Focused Energy Inc., 11525-B Stonehollow Drive, Suite 200, Austin, Texas 78758, USA.

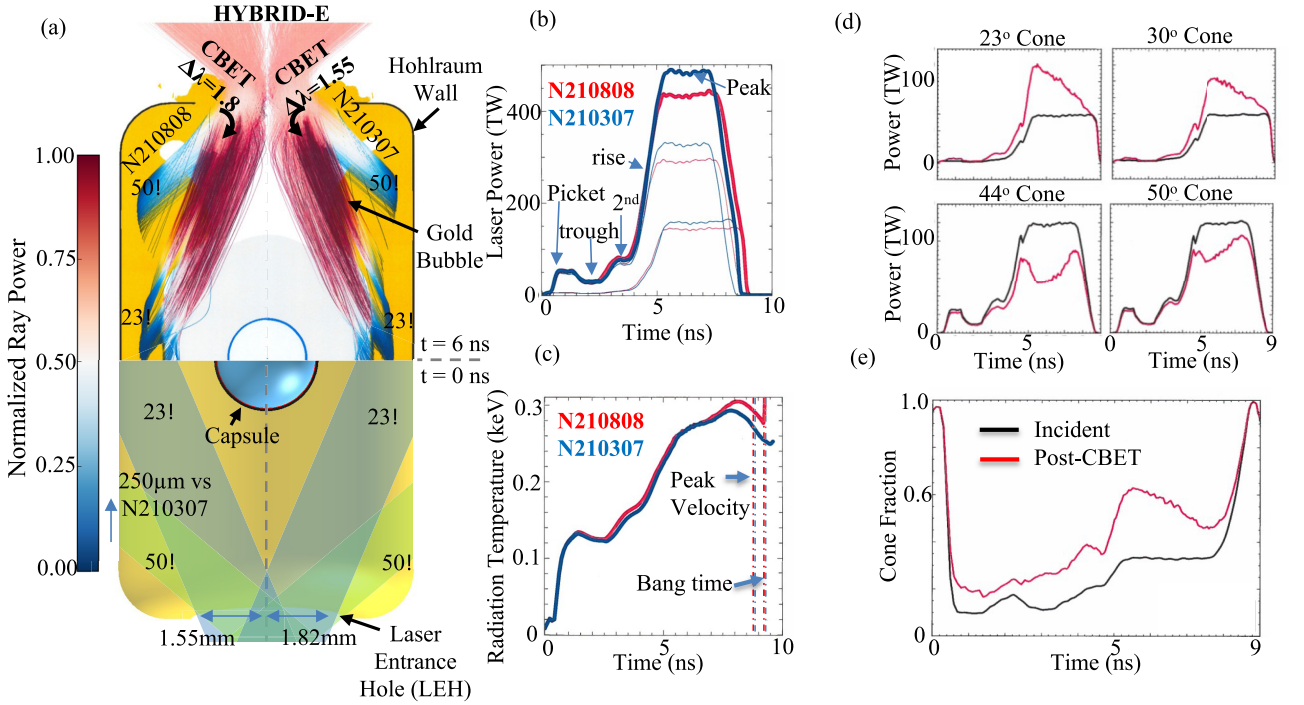

FIG. 1. (a) Top: Calculated positions of the wall and capsule materials [gold-lined depleted uranium hohlraum (orange), HDC ablator (light gray), and DT ice layer (blue)] at peak power (6 ns) from radiation-hydrodynamic HYDRA simulations with simulated laser rays colored by relative power overlaid. Implosion symmetry control is accomplished via cross-beam energy transfer (CBET) in low-gas-filled (~0.3 g/cm^3) hohlraums [6] from the "outer" laser beams (44.5° and 50°) to the "inner" beams (23° and 30°) by detuning the wavelengths relative to each other ($\Delta\lambda$). (a) Bottom: Hybrid-E target geometry at $t = 0$ with laser beam pointing (laser cones are labeled by their respective polar angle) for the new (N210808, left) and previous (N210307, right) configurations. (b) The total (thick curves), "outer" cone (thin middle curves), and "inner" cone (thin lower curves) laser powers vs time (i.e., pulse shape) for experiments N210808 (red) and N210307 (blue). The balancing of power between the "outer" and "inner" cones together with CBET is tailored to give precise control of the time-dependent radiation drive symmetry. (c) Simulated hohlraum internal radiation temperature, T_{rad}, histories for N210808 (red) and N210307 (blue). The extended T_{rad}, for N210808 compared to N210307 results in increased late-time ablation pressure and reduced "coast time." The near vertical rise of the T_{rad} at $t \sim 9.2$ ns seen in the red curve is reheating of the hohlraum from the capsule fusion output. "Bang times" or time of peak neutron production and times of peak implosion velocity are also denoted. (d) Calculated change in cone powers as a result of CBET moving power from the "outer" beams to the "inner" beams, incident in black and post-CBET in red. This calculation uses multipliers on the incident powers to match experimental tuning data [7]. (e) Ratio of the "inner" cone power to total laser power for the incident pulse (black) and post-CBET pulse (red) from the calculation in (d). See the text for more information.

and discussion of ignition criteria together with the historical perspective [10]. These experiments used the indirect drive approach [11–13] where an x-ray radiation source is generated via laser irradiation of a high atomic number cylindrical can, or hohlraum (see Fig. 1), and is used to heat and ablate the outside of a spherical capsule filled with DT fuel in the center of the radiation cavity. The ablation process accelerates the remaining capsule mass and DT fuel inward at high velocities doing work on the central hot spot, compressing and heating it. The plasma is confined inertially by the dense fuel surrounding the hot spot for a duration of time, releasing fusion energy until it explodes and cools. The spherical integrity of the imploding capsule is important for doing efficient work on the central hot spot [14–17] and requires a high degree of control and precision in both the intrinsic asymmetries that can result from the hohlraum and capsule configuration as well as the unintentional odd mode asymmetries. In addition, extra radiative loss in the system from hydrodynamic instabilities seeded by engineering features and material density gradients [18–21] can result in the mixing of capsule material with the compressed DT and central hot spot, reducing the compression and temperature. Designing an implosion that satisfies the conditions to do sufficient work on the implosion, while also controlling hydrodynamic instabilities and spherical symmetry, requires finesse and engineering control.

Initial experiments at the NIF [13] laid the groundwork for the technology and understanding, but were impacted by low-mode asymmetries which reduced the implosion efficiency, as well as hydrodynamic instabilities and sensitivity to perturbations caused by the capsule support tent [23]. Follow-on experiments to improve the hydrodynamic stability [18] by increasing the first shock ablation pressure enabled pushing the implosion to higher velocities before the capsule support tent perturbation eventually limited performance. Development of hohlraums with reduced He gas-fill density [24–26] resulted in higher laser coupling to the radiation cavity which enabled fielding larger hohlraums and better control of symmetry.

These experiments also used high-density carbon (HDC), or diamond, ablators, vs plastic, which resulted in less sensitivity to the capsule support tent perturbation and achieving higher hot-spot pressures [27–30]. However, these designs were already using the full laser energy and power of NIF but did not achieve sufficient energy coupling to the hot spot for α particle self-heating to sufficiently overcome losses for ignition to occur. See Ref. [10] for a more detailed description of the history and development of the program, understanding, and technology.

II. DESIGN IMPROVEMENTS

This paper reports on further optimizing the Hybrid-E [7,31,32] design (Fig. 1) which increased the amount of energy delivered to the hot spot by increasing the size of the implosion (15%) compared to previous experiments [27–30]. This design was part of the Hybrid strategy [33,34] to increase the scale (S) of the implosion for more energy coupled to the hot spot. The challenge of increasing initial capsule radius with fixed available laser energy is the potential loss of energy density. To do this, the Hybrid-E design [7,31,32] also balanced key metrics important for maintaining high hot-spot pressures such as the compressibility of the fuel ("adiabat" = plasma pressure/Fermi pressure), v_{imp}, implosion symmetry, hydrodynamic stability, and the late-time ablation pressure from the drive (related to "coast time" [35]) within the current confines of NIF. The "coast time" and stability were further optimized on experiment N210808 [36] compared to the predecessor experiments.

The increase in performance at fixed laser energy compared to previous designs is shown in Fig. 2 together with the theoretical hydrodynamic scalings of the highest performers from the previous designs. Figure 2 shows that much higher laser energies would have been required to produce $>$ MJ of fusion energy with no additional design changes and direct hydrodynamic scalings [37] to larger implosion scale from the prior designs. Advances in the understanding of symmetry control in low gas-fill hohlraums [38] and development of cross-beam energy transfer (CBET) in low gas-filled hohlraums through wavelength detuning [6] were essential improvements that enabled increasing the capsule scale in more efficient hohlraums to achieve this optimization. The lower density gas-filled hohlraums resulted in more effective symmetry control with modest amounts of wavelength separation while also achieving high levels of laser light coupling to the hohlraum, ~96%–99%; see the Appendix for the measured laser back-scattering on N210808. Previous high-gas filled hohlraums [13], however, displayed significant amounts of stimulated Raman and Brillouin back-scattering (~15%–20% of the incident laser energy), which resulted in a less efficient hohlraum and large amounts of wavelength separation to control the symmetry.

Following previously reported Hybrid-E experiments that reached the burning plasma regime [32,39,40], simulations indicated that further optimization of the coast time and hot-spot pressure could be achieved by increasing the late-time ablation pressure [35] (see Table I), which motivated this work.

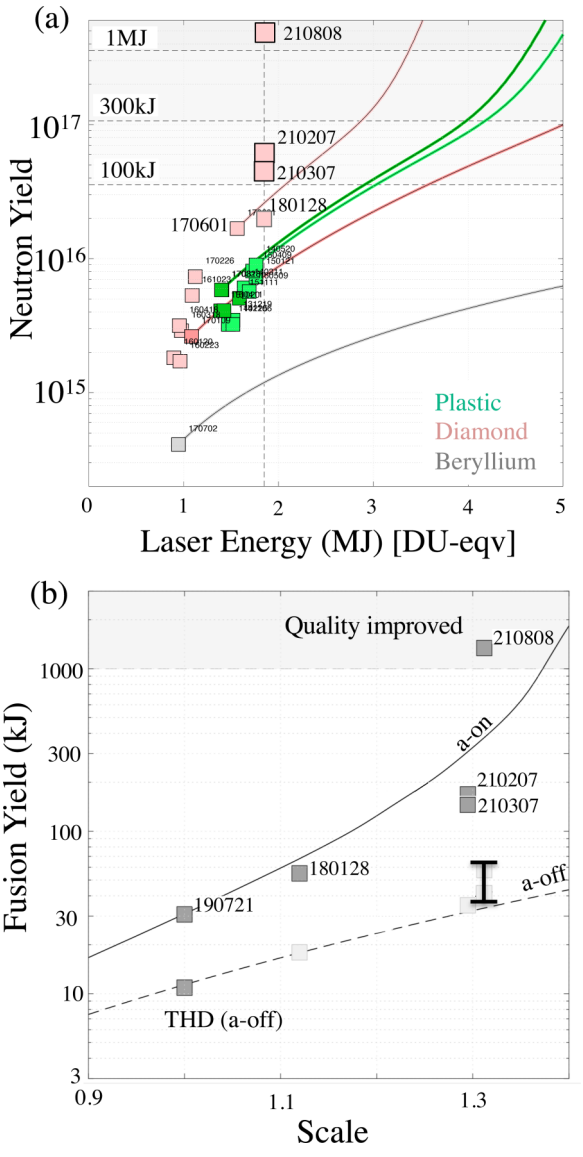

FIG. 2. (a) Neutron yield as a function of laser energy for diamond (pink), plastic (green), and beryllium (gray) ablator designs. Hybrid-E experiments (e.g., N210207, N210307, and N210808) show the improvement in performance at fixed available laser energy through design changes to increase the scale of the implosion while maintaining high hot-spot pressures. The curves are direct hydrodynamic scalings from best performing smaller scale designs which require more laser energy to increase implosion scale. The Hybrid-E experiments are notably higher than a direct scaling of previous smaller scale diamond ablator designs. (b) Fusion energy as a function of scaled DT ice mass showing that, in addition to being able to field a larger scale implosion at fixed laser energy, the quality of the implosion compared to a hydrodynamic scaling of Bigfoot experiment N180128 [22] was improved on N210808. The upper points are the measured yields, which include the impact of α heating (α-on), and the lower curve uses calculations to remove the impact of α heating (α-off), verified in a THD experiment at 1.0 scale (dark point) and calculated otherwise (light gray points).

A. "Coast" improvement

In this work, the late-time ablation pressure (or "coast time") was further optimized by reducing one of the main

TABLE I. Simulation metrics for N210808 compared to burning plasma experiments (N210207, N210307) and measurements. DSR is defined as the ratio of the 10–12 MeV neutrons to the 13–15 MeV neutrons. Burn-off metrics correspond to calculations where the α heating is artificially turned off, $P_{\rm abl}$ is the ablation pressure, and $E_{\rm cap}$ is the amount of energy absorbed by the capsule. G is gain of fusion energy over the amount delivered to the DT fuel, capsule, and target assembly.

Quantity	$N210207_{\rm Data}$	$N210207_{\rm Sim}$	$N210307_{\rm Data}$	$N210307_{\rm Sim}$	$N210808_{\rm Data}$	$N210808_{\rm Sim}$
			Setup			
Laser power, $P_{\rm laser}$ (TW)	470	470	487	487	441	441
Laser energy, $E_{\rm laser}$ (MJ)	1.93	1.93	1.909	1.909	1.917	1.917
Hohlraum diameter (mm)	6.4	6.4	6.4	6.4	6.4	6.4
Hohlraum length (mm)	11.24	11.24	11.24	11.24	11.24	11.24
Laser entrance hole (LEH) diameter (mm)	3.64	3.64	3.64	3.64	3.1	3.1
Wavelength separation, $\Delta\lambda$ (Å)	1.55	1.55	1.55	1.55	1.8	1.8
			Observables and Calculated Hohlraum and Implosion Metrics			
Bang time (BT) (ns)	9.09 ± 0.03	9.05	9.31 ± 0.03	9.35	9.26 ± 0.03	9.26
Fusion yield, $Y_{\rm total}$ (MJ)	0.170	0.157	0.145	0.122	1.37	1.353
DT ion temperature, $T_{\rm DT}$ (keV)	5.66 ± 0.13	6.37	5.55 ± 0.11	5.78	10.9 ± 0.4	11.3
DD ion temperature, $T_{\rm DD}$ (keV)	5.23 ± 0.16	5.84	4.87 ± 0.14	4.91	8.94 ± 0.4	8.7
Thermal ion temperature, $T_{\rm th}$ (keV)	n/a	5.5	n/a	5.24	n/a	9.83
Down-scattered ratio, DSR (%)	3.16 ± 0.16	3.58	3.49 ± 0.16	3.45	2.87 ± 0.24	3.09
Burn width, $\tau_{\rm BW}$ (ps)	103 ± 25	110	138 ± 20	110	89 ± 5	78
Maximum implosion velocity, $v_{\rm imp}$ (km/s)	n/a	393	n/a	387	n/a	391
Time of peak velocity, $t_{\rm vimp}$ (ns)	n/a	8.63	n/a	8.9	n/a	8.8
Remaining ablator mass (%)	n/a	4.7	n/a	5.7	n/a	4.8
Max radiation temperature, $T_{\rm r,max}$ (eV)	302	295 (internal)	294	294 (internal)	307	305 (internal)
Radiation temperature at BT, $T_{\rm r,BT}$ (eV)	n/a	260 (internal)	n/a	254 (internal)	n/a	276 (internal)
Radiation temperature at $t_{\rm vimp,max}$ (eV)	n/a	279 (internal)	n/a	270 (internal)	n/a	291 (internal)
DT fuel adiabat	n/a	$\sim$3	n/a	$\sim$3	n/a	$\sim$3
			Coast Metrics			
Radius peak velocity$_{\rm LimbMin}$ (μm)	n/a	195	n/a	211	n/a	185
Coast time, $t_{\rm coast}$ (ns)	1.04	1.05	1.2	1.2	0.86	0.86
$P_{\rm abl} \sim 145(T_{r,t_{\rm vimp}}/300)^{2.4}$ (Mbar)	n/a	121.8	n/a	112.6	n/a	134.8
$P_{\rm abl} \sim 145(T_{r,avg(t_{\rm vimp,max})}/300)^{2.4}$ (Mbar)	n/a	124.3	n/a	115.4	n/a	132
			"Burn-off" (No-α Heating) Metrics			
Fusion yield, no-α $Y_{\rm total}$ (MJ)	n/a	0.024	n/a	0.03	n/a	0.044
Hot-spot pressure, no-α $p_{\rm hs}$ (Gbar)	n/a	170	n/a	194	n/a	252
DT ion temperature, no-α $T_{\rm DT}$ (keV)	n/a	4.82	n/a	4.57	n/a	4.9
Hot-spot areal density, no-α $\rho R_{\rm hs}$ (g/cm^2)	n/a	0.26	n/a	0.29	n/a	0.26
			Hot-Spot and Ignition Metrics			
Hot-spot pressure, $p_{\rm hs}$ (Gbar)	351 ± 23	290	353 ± 23	281	569 ± 61	442
Hot-spot internal energy, IE$_{\rm hs}$ (kJ)	17.4 ± 1.1	19	14.6 ± 0.9	16	55 ± 6.0	61.5
Ignition metric ($E_{\rm hs}P_{\rm hs}^2$) norm. to N210307	n/a	1.26	n/a	1.0	n/a	9.5
Hot-spot areal density, $\rho R_{\rm hs}$ (g/cm^2)	0.37 ± 0.4	0.38	0.38 ± 0.02	0.40	0.44 ± 0.05	0.426
Hot-spot volume, V ($10^5 \mu$m^3)	3.3 ± 0.3	2.7	2.7 ± 0.3	2.3	6.4 ± 0.75	9.1
d^2T_{DT}/dt_{BT}^2(keV/ns^2)	n/a	$\sim$-2	n/a	$\sim$-2	n/a	$\sim +6$
Yield amplification, $Y_{total}/Y_{total,no-\alpha}$	n/a	6.7	n/a	4.1	n/a	30.6
$G_{\rm fuel} = Y_{\rm total,exp}/$kinetic energy$_{DT}$	$7.5^{+0.54}_{-0.82}$	10.5	$7.77^{+0.55}_{-0.82}$	8.7	$75.6^{+3.6}_{-5.6}$	84
$G_{\rm capsule} = Y_{\rm total,meas.}/E_{\rm cap}$	0.75 ± 0.05	0.8	0.69 ± 0.05	0.7	5.8	6.3
$G_{\rm target} = Y_{\rm total,meas.}/E_{\rm laser}$	0.089	0.09	0.075	0.08	0.72	0.71
Generalized Lawson criterion$_L$[a] [41]	< 1 [10]	0.66	< 1 [10]	0.61	> 1 [10]	1.7
Generalized Lawson criterion$_H$ [42]	< 1 [10]	0.5	< 1 [10]	0.37	> 1 [10]	2.2

[a]The method in Ref. [41] uses quantities for pressure and radius that are fusion burn-weighted in time and space, vs the reported numbers in the table that are spatially burn-weighted quantities at the time of peak neutron production.

sources of radiation loss in the hohlraum, the laser entrance holes (LEHs) from 3.64 mm diameter (N210307) to 3.1 mm diameter (N210808); see Fig. 1(a) (bottom) for schematics of N210307 and N210808. The efficacy of using a smaller LEH to improve hohlraum efficiency was first tested in tuning experiments [43,44] which used a previous 1100 μm scale Hybrid-E design [7] which used the same laser beam pointing and hohlraum configuration as the burning plasma Hybrid-E

design [32,39]. These experiments verified increased radiation temperature and energy coupling with adequate low-mode symmetry control at larger scale. For the N210808 design, the reduction in radiation losses with the smaller LEH was used to operate at lower peak power for N210808 vs N210307 while still achieving similar radiation temperature (T_{rad}) [Fig. 1(c)], implosion velocity, and ablator mass remaining, but significantly reducing the "coast time" (see Table I). Here the saved energy from operating at lower power was used to extend the pulse duration at the same total laser energy to increase the late-time T_{rad} and ablation pressure.

The value t_{coast} is defined as the difference in bang time and the time where the laser power falls off to half maximum after the peak of the laser pulse, which was reduced by 40% compared to N210307 for N210808 (∼350 ps shorter). The radius of peak velocity (RPV) [45] is another metric for reduced "coast time," which becomes smaller as the "coast" is reduced. The RPV for N210808 was reduced by ∼30 μm compared to N210307 leading to a predicted increase in up to 50 Gbar of no-α (without the impact of α heating) hot-spot pressure and is defined in Table I as the minimum transmission of an in-flight radiograph of the dense fuel and shell.

Other "coast" metrics were notably improved for N210208 vs N210307, including the late-time ablation pressure calculated using the simulated radiation temperature at time of peak implosion velocity (t_{vimp}) and maximum radiation temperature. The calculated internal radiation temperature was ∼20 eV higher for N210808 compared to N210307 at "bang time," time of maximum neutron production. The estimated increase in EP^2, an ignition metric [37,46], was >7–10× the previous burning plasma experiments and ∼40% higher for no-α EP^2 (no-α removes the impact of α heating on calculated hot-spot metrics).

B. Low-mode symmetry

Reducing the size of the LEH required moving the position of the 50° laser beams toward the midplane of the hohlraum [43,44] so they are not absorbed unintentionally by the edge of the LEH; see Fig. 1(a) (bottom). This creates more overlap between the "outer" laser beams (44° and 50°), which causes the "gold bubble" (ablated Au wall plasma) to ingress further, which can inhibit the "inner" laser beams (23° and 30°) from reaching the interior of the hohlraum. This can be seen in Fig. 1(a) (top), which shows radiation hydrodynamic simulations (HYDRA) [47] of the integrated designs for N210808 (left) and N210307 (right) at 6 nanoseconds after the start of the laser pulse. The relatively smaller gap between the capsule and hohlraum wall gives less physical space for the laser beams to propagate in and more interaction with the ingress of hohlraum wall plasma, resulting in an energetically undesirable oblate asymmetric implosion—asymmetry wastes implosion kinetic energy, and time variation fluctuations in the radiation drive symmetry can cause large ρR variations in the compressed DT which reduces the implosion efficiency and confinement time.

To regain sufficient drive at the waist of the hohlraum, the amount of light transferred from the "outer" to "inner" beams (CBET) was increased by additionally detuning their relative wavelengths ($\Delta\lambda$ = "Inner" beam–"Outer" beam before laser frequency tripling) [6,48–50] from $\Delta\lambda = 1.55$ Å for N210307 to $\Delta\lambda = 1.8$ Å for N210808. The additional transfer can be seen in the simulated laser rays colored by the spatially varying power after transfer for the two configurations in Fig. 1(a) and in the calculated post-CBET vs incident laser powers by cone in Fig. 1(d). This can also be seen in Fig. 1(e), which shows a larger cone fraction (ratio of "inner" power to total power) post-CBET (red) vs incident (black).

The intentional increase in energy transfer during the peak of the pulse also results in more transfer during the "foot" of the pulse (before the rise to peak power), which was then reoptimized by adjusting the time-dependent foot cone fraction [6,7,32]. This is done by changing the ratio of "inner" beam power to total power using radiation hydrodynamic simulations. Figure 3(a) shows the calculated P1, P2, and P4 Legendre moments of the radiation drive for N210808, the scaled laser pulse, and the cone fraction as a function of time. Since the outers are "drooping," or ramping down, late in time while the "inner" beams are being held on, this causes the late-time increase in cone fraction. This "drooping" was incorporated into the design to enable using the full NIF energy and power on all 192 laser beams, increase the late-time ablation pressure, and mitigate potential laser backscattering out of the hohlraum late in time from the "outer" beams which interact with the high-Z expanding wall plasma; see the Appendix. The cone fraction in the peak was 33% and was also chosen (together with the shape of the droop) to enable the full use of NIF, which results in a P2 flux asymmetry swing during to the peak from waist to pole hot as the wall ingresses. If this swing can be balanced, the imploding shell and hot-spot symmetry can be maintained. Simulations were used to design the "foot" symmetry, and work is currently being done to benchmark the flux asymmetry calculations in the rise and peak for the N210808 platform.

Since late-time laser beam propagation through the plasma filled hohlraum is difficult to model, a data-driven model [38] was used together with an experimental playbook of delta hot spot P2 vs $\Delta\lambda$ to select the wavelength separation for N210808 [Fig. 3(b)] and tested in a symmetry-tuning experiment [9] prior to N210808. The y axis is the amount of observed increase in hot spot P2 (more prolate due to more drive on the hohlraum waist) compared to the calculated P2 using the model [38] at $\Delta\lambda = 0$ Å for the hohlraum design parameters and fielding conditions. Figure 3 includes several 1050 μm inner radius Hybrid-E experiments and symcap experiment N210601 [9], which used the same hohlraum configuration as N210808 [9]. This experiment did not include the DT payload and is more prolate compared to a DT at the same wavelength separation.

C. Additional changes

Other aspects impacting the quality of the implosion were improved for N210808 compared to predecessor experiments (N210307 and N210207), including a more stable Atwood number at the DT fuel-ablator interface, improved diamond ablator quality [9,20], and reduced DT fill-tube diameter from 5 μm to 2 μm [21,52]. The Atwood number is an important parameter which determines the growth of hydrodynamic instabilities [Rayleigh-Taylor (RT)] and is defined

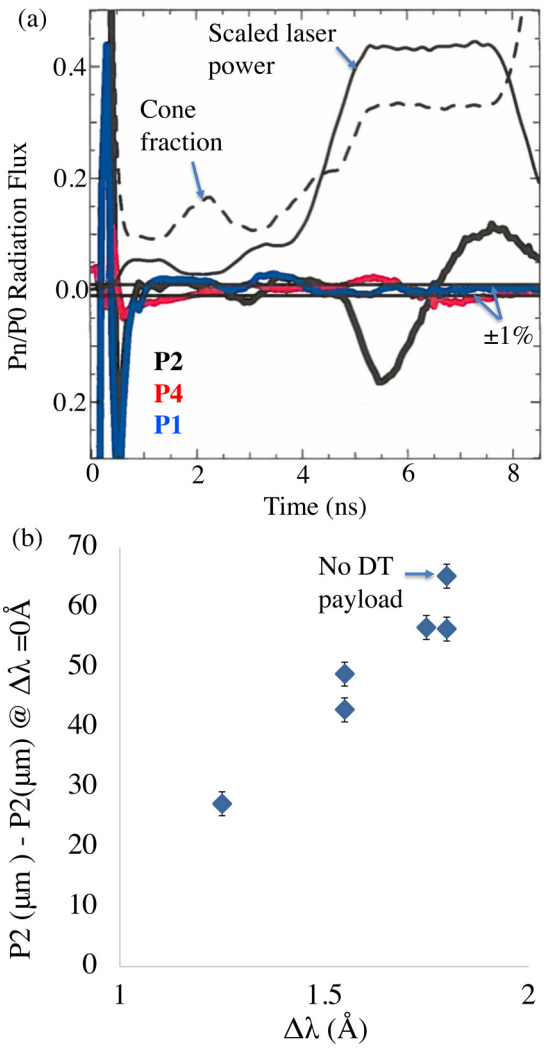

FIG. 3. (a) Simulated Legendre decomposition of the radiation flux asymmetry (Pn = P1, P2, and P4) for N210808 plotted together with the scaled laser power as a function of time, and cone fraction (ratio of "inner" laser cones to total power) as a function of time. Also denoted is the range of ±1% radiation flux asymmetry. The calculated radiation flux symmetry is within specification during most of the pulse for P1 and P4. The P2 decomposition is within the specification during the "foot," until the rise to peak power, but is allowed to swing during the peak of the pulse (see the text). These calculations do not adjust the drive of the "inner" cones and overestimate the P2 swing in the rise to peak. (b) Observed increase in hot spot P2 (more prolate) for a given amount of wavelength separation ($\Delta\lambda$) over the calculated P2 at $\Delta\lambda = 0$ Å using the Callahan *et al.* semiempirical model [38].

as $A = (\rho_1 - \rho_2)/(\rho_1 + \rho_2)$, where ρ_1 is the density of the compressed DT fuel and ρ_2 is the density of the remaining ablator material. When this parameter is small, the accelerating fuel-ablator interface is more stable, reducing growth of the RT instability. The improvement in quality on performance for N210808 compared to the previous burning plasma experiments (N210207 and N210307) can be seen in Fig. 2(b), which shows fusion energy produced as a function of scaled DT ice mass together with the theoretical hydrodynamic scaling (gray curves). The performance of N210808 exceeds the hydrodynamic scaling from smaller scale Bigfoot diamond ablator experiments [22], accounting for the scaled DT fuel mass. The N210808 design used a thicker DT ice layer compared to a hydrodynamic scaling of Bigfoot (~30% increase in DT thickness for a ~10% increase in scale), which can protect the "hot spot" from high-Z ablator mixing, translating to better implosion quality, but also had a lower design fuel adiabat. Future experiments will test sensitivities to the trade-offs in these design parameters for N210808 (adiabat and DT thickness). Experiments N210207 and N210307 also used a thick (65 μm) DT ice layer but may have been limited by capsule quality or nonoptimal "coast time." The thicker ice of the N210808 design was motivated by successful tests to mitigate the impact of observed capsule quality defects in larger scale 1100 μm Hybrid-E experiments [7,31]. Increasing the ice thickness is a trade-off with implosion velocity and ablator mass remaining at a given implosion velocity. Thicker ice layers require longer laser pulses for the shocks to transit the ice, which burns off more ablator mass. Maintaining sufficient ablator mass is also important for stability and confinement, and sensitivity to ablator thickness and mass remaining for N210808 will be studied in future experiments.

Figure 4 shows the hohlraum and capsule configuration for N210808 and capsule configurations burning plasma experiments N210207 and N210307. For all three experiments the hohlraum was gold-lined depleted uranium (Au-lined DU), 6.4 mm in diameter and 11.24 mm in length, with a helium gas fill density in the hohlraum of 0.3 mg/cm^3. Gold-lined DU hohlraums require less energy in the beginning of the pulse (picket) to achieve the same radiation temperature compared to unlined DU hohlraums, which slows down the ingress of the wall bubble (see the low mode symmetry Sec. II B) while providing a higher radiation drive in the peak of the pulse compared to solid Gold hohlraums due to the higher albedo. The laser entrance hole was 3.64 mm in diameter for N210307 and N210207 and 3.1 mm in diameter or N210808 (see also Table I). An improved diagnostic window configuration to reduce odd mode radiation drive asymmetries [16] was used on N210808 but not N210307 or N210207. The diamond ablators consisted of an inner undoped diamond layer, a W-doped diamond layer at larger radius, and an outer undoped diamond layer. The crystal structure was microcrystalline diamond (MCD) for N210207 (fabrication batch identification number KC720) and nanocrystalline (NCD) for N210307 (batch KC461) and N210808 (batch KC789). The ablator thickness ranged from ~76 μm to 80 μm due to the difference in mass density of the ablator, ~3.5 g/cm^3 for MCD, and ~3.32 g/cm^3 for NCD.

The N210808 and N210307 capsules had a high level of tungsten dopant (~0.42%–0.44% W), designed to improve the Atwood number at the accelerating fuel-ablator interface by maintaining the ablator density relative to the compressed DT fuel density; see Fig. 5 (blue is N210207 0.28% W-doped HDC and red is N210307 0.44% W-doped HDC). Diamond ablator batch KC461 was the first >0.4% W-doped diamond batch and the first NCD batch to be tested at the NIF in earlier Hybrid-B experiments [20,53]. However, this batch contained thousands of voids, which can seed hydrodynamic instabilities [20]. The design for N210808 used a high-dopant ablator together with higher quality capsules (fewer defects)

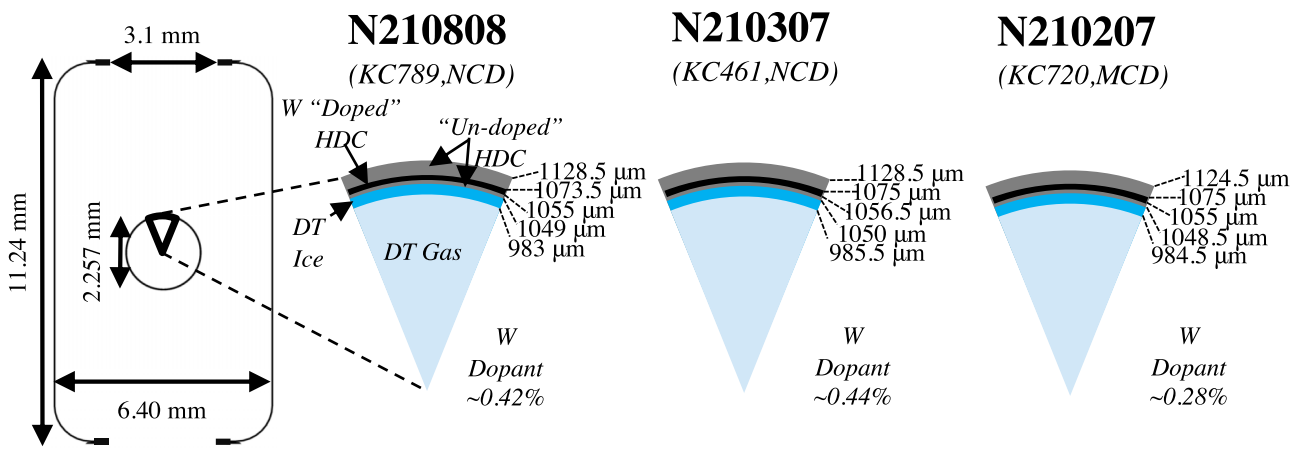

FIG. 4. Schematic of the N210808 Hybrid-E hohlraum and capsule configuration showing the nominal target dimensions for the hohlraum (left) and pie chart for the central DT-fuel filled capsules (right). Also shown are pie charts for N210307 and N210207. The diamond ablator consists of a ∼6 μm inner undoped HDC layer, followed by a tungsten (W)-doped HDC layer at larger radii and an outer undoped HDC layer. The crystal structure for the diamond ablators used in N210307 and N210808 was nanocrystalline diamond (NCD) compared to microcrystalline diamond (MCD) used in experiment N210207. The DT ice and gas core radii are also listed.

[9] and additionally improved the calculated stability at the DT-fuel ablator interface with the lower "coast" drive, being stable for nearly the entire acceleration phase (black curve). Improving Atwood number at the fuel-ablator interface with higher W-dopant capsules is generally a trade-off with growth factors for perturbations seeded at the ablation front [54]. To balance this tradeoff, gold-lined DU hohlraums were chosen due to their higher level of M band (> 1.8 keV) in the radiation spectrum, which blows down the ablation front and reduces growth factors. Other intentional design changes include adjusting the length of the pulse before peak power (shortening the "trough" by 100 ps) to maintain equivalent shock timing, given the higher early-time radiation temperature, compared to N210307 [see Fig. 6(a) and Fig. 1]. The increase in early-time "picket" $T_{\rm rad}$ also helps with stability at the ablation front [18]. Figure 6(b) shows the radial pressure gradient as a function of time which enables tracking the three shocks launched by three distinct power steps in the laser profile, moving through the ablator and DT ice. The plot on the left shows the shock trajectories in radius and time for the previous N210307 platform along the equator, where the merger of the first and second shocks is ∼10 μm inside the DT ice from the ice-gas interface. This merger within the DT ice increases the adiabat by ∼0.3–0.5 compared to merging shocks 1 and 2 at the ice gas interface (where the calculated adiabat of N210808 is 3–3.3). The adiabat is also set by the strength of the first shock and the rate of rise of the final shock due to reflection off of the ablation front of the rarefaction from the third shock. Here the higher M band of the Au-lined DU hohlraum compared to unlined-DU reduces steepness at the ablation front and results in a weaker reflected shock.

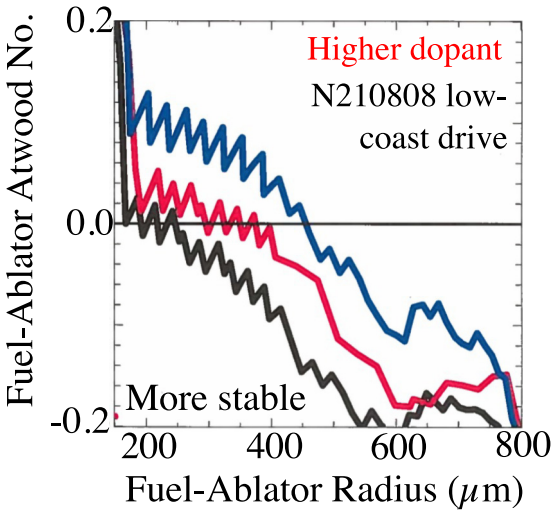

FIG. 5. Calculated DT fuel-HDC ablator Atwood number as a function of fuel-ablator radius for Hybrid-E designs using lower W-dopant diamond ablators (N210207 with 0.3% W dopant, blue) compared to higher W-dopant ablators in the longer "coast-time" configuration (N210307 with 0.44% W dopant, red). The improvement in Atwood number for the higher W-dopant ablators in the lower-coast design of N210808 is shown in black (KC789 with 0.42% W dopant). When the ablator density > the DT fuel density (negative values on the y axis) the implosion is more stable at the DT fuel-ablator interface.

While calculations predict higher performance by additionally reducing the adiabat from N210808 (shock mergers closer to the ice-gas interface), past studies have shown opposite trends experimentally due to complications at higher convergence [33]. Thus for the N210808 design which was meant to be primarily a test of "coast" time, the shock trajectories were maintained relative to the previous burning plasma experiments. Future experiments will test a reduction in adiabat from N210808. The preshot N210808 laser pulse request was designed to give similar shock timing to N210307 [middle plot of Fig. 6(b)] and the postshot as-delivered laser resulted in a slightly deeper 1–2 shock merger than the preshot calculation. Model validation for simulated shock trajectories for the N210808 configuration was not performed prior to the experiments, and work is ongoing to benchmark the calculations. Here we use earlier data from the Hybrid-E campaign [7] to calibrate the modeling.

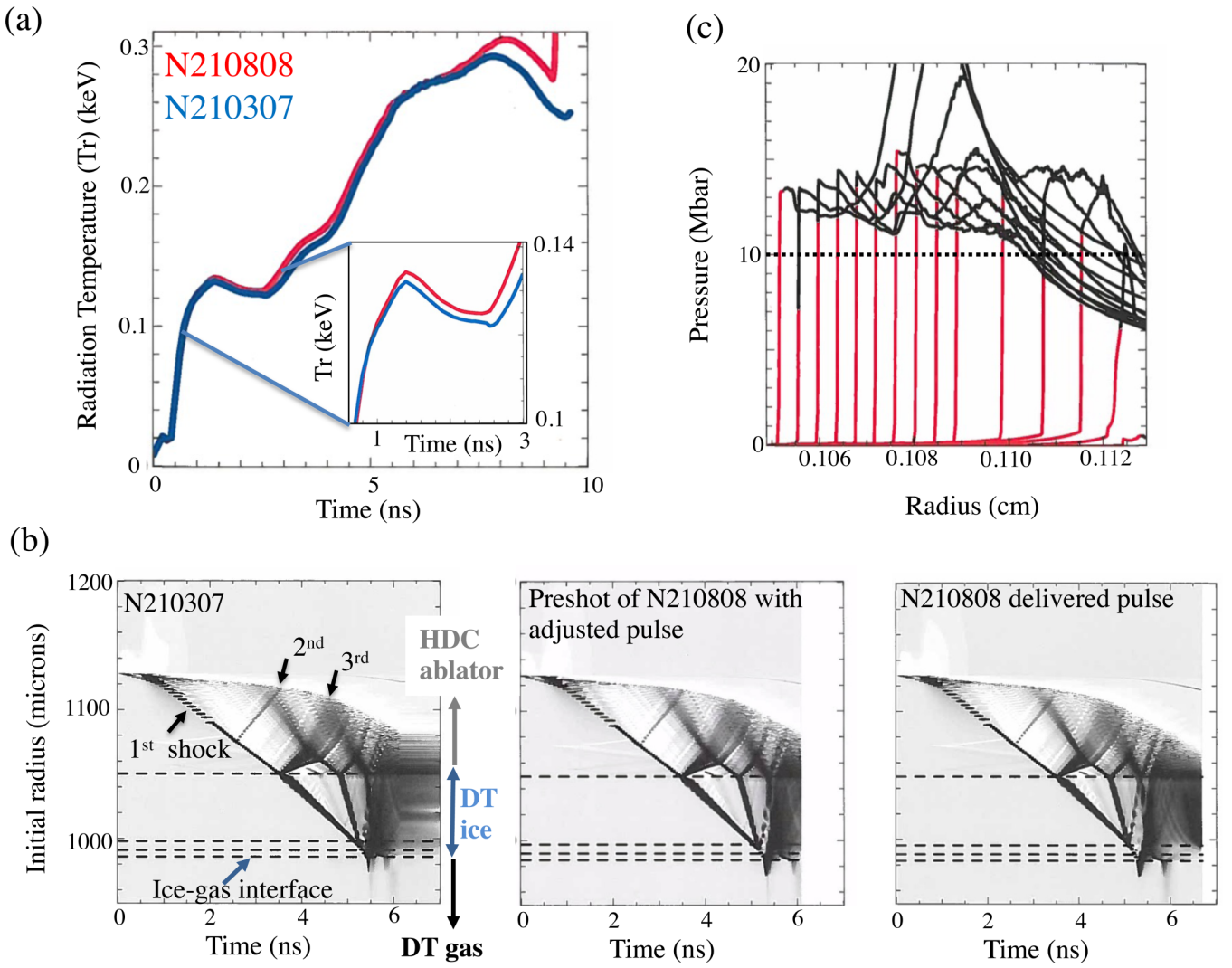

FIG. 6. (a) Simulated internal radiation temperature for N210808 (red) and N210307 (blue) where the inset is expanded on the first shock. (b) Radial pressure gradients of the three shocks launched by distinct changes in radiation temperature plotted as a function of initial radius vs time. The darker contours show the shock front moving through the various capsule layers (ablator, DT ice, and DT gas), which are denoted on the right-hand side. The ice-gas interface is also noted. The plot on the left-hand side is for experiment N210307, the middle is a preshot calculation for the adjusted N210808 pulse (see the text), and the right-hand plot is for the postshot delivered N210808 pulse. (c) Calculated leading shock front pressure in the diamond (red) is higher than the melting pressure for HDC along the shock Hugoniot (∼10–12 Mbar) [51]. The black curves denote where the temperature is > 3 eV behind the shock front.

Figure 6(c) shows the calculated leading shock pressure in the diamond ablator where each line corresponds to a different time as the shock moves through the diamond. The black curves overlaid denote where the temperature behind the shock is > 3 eV, sufficient to melt diamond. This design is calculated to have a high enough first shock pressure (> 10–12 Mbar) [51] to avoid refreeze of the diamond.

The laser power during the "peak" of the pulse (see Fig. 1) was reduced to increase late-time ablation pressure and reduce "coast" time; see the "Coast" improvement section, II.A. The level of reduced power was chosen to maintain sufficient ablator mass remaining of ∼5% to avoid burn-through and loss of stability and confinement, while also maintaining a comparable implosion velocity to the burning plasma experiments N210307 and N210207 (∼390 km/s; see Table I). Figure 7(a) shows the relationship between ablator mass remaining and implosion velocity for two capsule options [KC720 (red) and KC789 (blue)] in the small LEH configuration. Here the velocity was varied by adjusting the laser power in the peak of the pulse [Fig. 7(b)] while maintaining the full laser energy (1.9 MJ) through extending or contracting the "peak" duration.

III. RELATIVE IMPACTS OF CHANGES

The sensitivity of performance (total neutron yield) to changes made between the burning plasma regime (N210307) and N210808 calculated using HYDRA are shown in Fig. 8. These calculations use calibrated models for the capsule support tent and DT fill-tube perturbations, and include roughnesses at the ice and ablator interfaces (see the Appendix). The insets are "bang-time" images of the DT density (left)

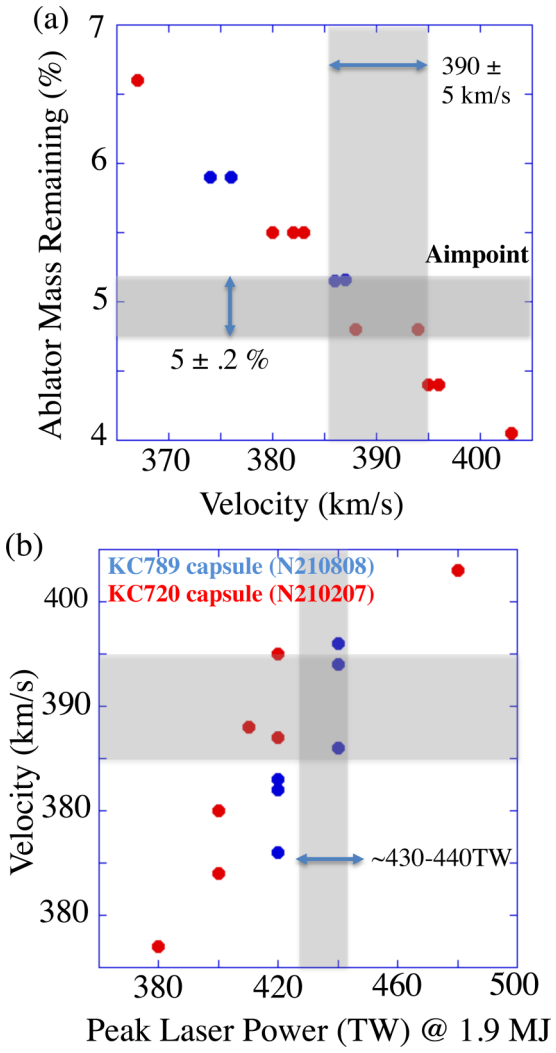

FIG. 7. Calculations of ablator mass remaining as a function of implosion velocity (a) and implosion velocity as a function of peak laser power (b) for preshot simulations of the N210808 hohlraum and LEH configuration for high (blue) and low (red) W-doped capsule batches (see Fig. 4). As the peak laser power is varied the total laser energy is conserved. The spread in velocities for a given peak laser power is a result of using a range to estimate uncertainty in the drive benefit of the smaller LEH (3.1 vs 3.64 mm) for the full 1.9 MJ laser energy, which was first fielded on this experiment N210808. The design point for N210808 was ~5% ablator mass remaining and ~390 km/s, which led to the 430 TW requested laser power (with 440 TW actually delivered on N210808).

and ion temperature (right) on a scale of ±70 μm. As the yield increases, the size of the hot spot increases as a result of burning into the fuel and compressed DT shell, which was observed experimentally on N210808 [9]. The blue dashed bars are measured yields for N210307 (dark blue) and N210808 (light blue). The dark blue bars represent postshot simulations of N210307 sequentially "walking" to the conditions of N210808 (postshot simulations of N210808 are the solid light blue bars).

Postshot simulations including all degradations for N210307 and N210808 are denoted by (a) and (g), respectively. Moving from left to right, the low-mode

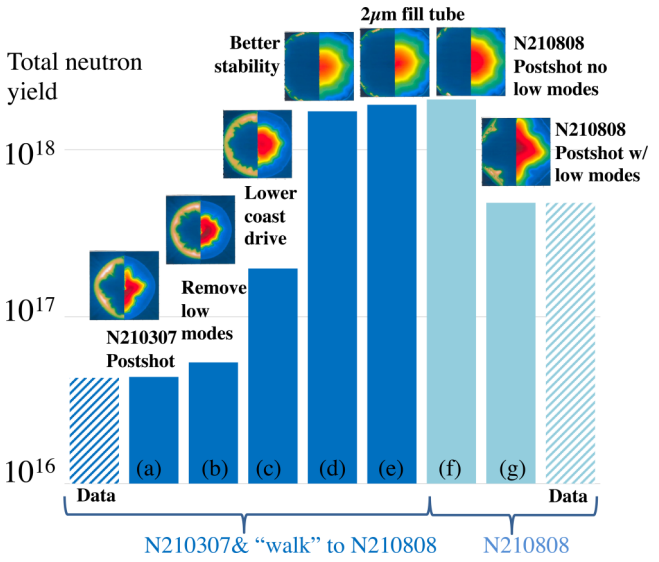

FIG. 8. Relative impacts: Simulations of the total neutron yield for the changes made between the burning plasma regime (N210307) and this paper (N210808) including the lower-coast radiation drive, DT fill-tube size change, stability improvement, and capsule quality change. Postshot simulations including all degradations for that experiment, (a) for N210307 and (g) for N210808, are compared to experimental data (slashed bars). See the text for a description of the relative changes between the bars. The insets are simulated images of the density (left) and ion temperature (right); see also the text.

radiation drive asymmetries are first removed from the postshot simulation of N210307 (b), which has a ~20% impact on performance for this platform. Then the lower coast drive used for N210808 was applied to this calculation (c) showing the impact of the increased late-time ablation pressure fielded on N210808, which was ~4×. The impact of stability improvements made between N210307 and N210808 (improvements to the Atwood number and capsule quality) were estimated by making adjustments to the fall-line mix model (see the Appendix), moving from bar (c) to bar (d). A ~5× increase in yield is estimated from the improvement in capsule quality, which was determined by comparing the fall-line model required to match the observed conditions of N210307 (see Table I) to a benchmarked fall-line model for prior experiments [55], which had higher intrinsic capsule quality (defects inside the ablator). Since N210808 was calculated to be stable for the entire acceleration phase, removing the fall-line mix model resulted in an additional ~65% increase in performance. The impact of the reduced DT fill-tube size (2 μm for N210808 and 5 μm for N210307) was a ~10% increase in performance for bar (e) compared to bar (d), which used a calibrated 2 μm fill-tube model.

A postshot calculation of N210808 without low modes from the radiation drive is denoted by bar (f) and with low modes from the radiation drive by bar (g), which had a higher impact on performance in this regime and for this order of applied perturbations. The order in which a perturbation is applied may influence its impact on performance. The final postshot simulation denoted by bar (g) also matched other experimental observables (see Table I) without the need for

applying a fuel-ablator fall line mix model. This figure shows that the main contributors for the higher performance of N210808 vs N210307 were the design changes that produced a lower-coast implosion, more stable fuel-ablator interface, and improved diamond ablator quality which led to higher compressions [measured through the down-scattered neutron ratio (DSR); see Table I].

IV. SIMULATED HOT-SPOT CONDITIONS AND IGNITION METRICS FOR N210808

Simulations support N210808 being in a fundamentally new regime as compared to the burning plasma experiments (e.g., N210307 and N210207) and previous α-heating experiment N170601. This can be seen in Fig. 9(a), which shows the evolution in time of the hot-spot ion temperature as a function of hot spot ρR with the time direction noted on the curves with arrows. Also shown is a dashed curve which corresponds to the temperature and ρR conditions where α heating and losses in the system (radiative losses, conduction losses, and explosion phase cooling) roughly balance [37]. For N170601 the fusion yield exceeded the kinetic energy of the DT, but the α heating was not sufficient to overcome the losses and the hot spot disassembles to lower ρR and ion temperature. Burning plasma experiment N210307 had a greater amount of α heating that dominated the hot-spot energy balance, which started in its creation with a higher initial ion temperature as a result of the design changes, but the α heating was not sufficient to overcome the losses for a long enough duration to provide significant α-bootstrap heating. The N210808 experiment shows a substantial increase in hot-spot temperature and ρR and a reversal of the trajectory where the hot spot continues to increase in temperature on expansion. Here the extra initial confinement and α heating allow the temperature overcome losses and increase significantly.

Simulations of N210808 hot-spot energy balance support the creation of an "igniting" plasma. When the α particle heating is greater than the initial work done on the plasma as well as the energy loss mechanisms, and for a long enough duration of time (confinement time), the plasma "ignites" and a thermodynamic instability or tipping point in DT plasma self-heating occurs; see [10]. We use these detailed postshot simulations that match experimental observables to assess the energy balance in the hot spot. Figure 9(b) shows the cumulative hot-spot energies for N210808 as a function of time including the PdV (P: pressure; dV: volume change) work being done on the hot spot (black), internal hot spot energy (blue), radiative loss from the hot spot (red), and conduction losses (magenta). The PdV work term also becomes a loss mechanism when the high-pressure hot spot expands, or explodes, due to its own pressure. This happens when the PdV cumulative energy starts to decrease just after the implosion has reached minimum volume and eventually becomes negative. It can be seen in Fig. 9 that the amount of heating from α particles far outweighs the amount of work being done on the hot spot. Early in time the internal energy of the hot spot tracks the work being done on the hot spot but increases beyond this starting at about 9.1 ns due to the additional α-particle heating. As the other loss terms start to increase (radiative loss, conduction losses, and explosion phase losses) the internal energy continues to increases and reaches peak burn well after the time of minimum volume, when PdV changes sign from positive to negative and burns into the surrounding denser fuel as the implosion is exploding. This indicates that significant α-particle bootstrap heating of the hot spot has occurred and that the hot spot has ignited.

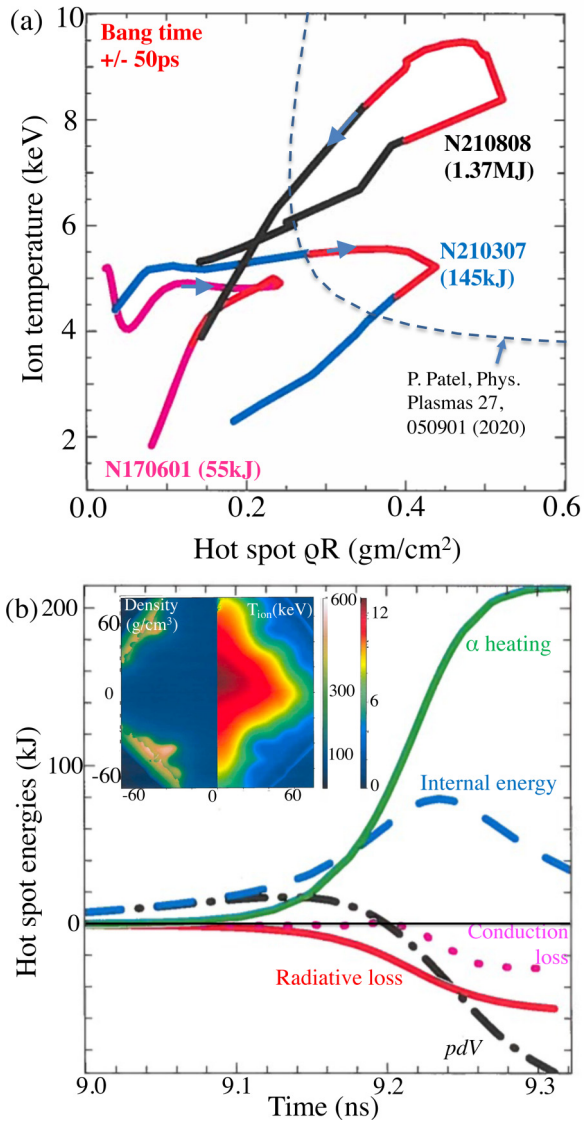

FIG. 9. (a) "Hot-spot" ion temperature and ρR evolution as a function of time for α-heating experiment N170601 compared to burning plasma experiment N210307 and ignition by Lawson criterion experiment N210808. The direction of increasing time is shown with the arrows on the curves, and the overlaid red curves denote "bang time" (peak neutron production) and ± 50 ps. The dashed curve is a theoretical model for conditions where the α heating balances the loss terms. (b) Calculated hot-spot energy partition as a function of time: PdV work on the hot spot [black (dot-dashed)], energy deposited by α heating (green), radiative (red), and conduction [magenta (dotted)] energy loss, and hot-spot internal energy [blue (dashed)]. Note that the negative PdV work is a loss term that is comparable to the radiative loss and exceeds the conduction loss by the time of peak neutron production. Inset: Simulated density (left, g/cm^3) and ion temperature $T_{\rm ion}$ (right, keV) at the time of peak neutron production. Inset spatial scale in microns.

Several simulated metrics also support that N210808 has crossed the ignition threshold. The calculated ratio of fusion yield produced for N210808 to the amount of work done on the hot spot, or fuel gain, is $G_{\text{fuel}} \sim 80\times$, which is a $\sim 10\times$ increase over the predecessor experiments (see Table I). The capsule gain, or fusion energy produced compared to the amount of energy absorbed by the capsule to drive the implosion, was $G_{\text{capsule}} \sim 6\times$ for N210808, which was the first experiment to achieve $G_{\text{capsule}} > 1$. The high level of calculated yield amplification, ratio of the yield to the expected yield without α heating, of $\sim 30\times$ compared to predecessor experiments ($\sim$4–7) is also a signature of an igniting plasma.

Other metrics such as the generalized lawson criterion (GLC_H [42] and GLC_L[41]) are calculated to be greater than one for N210808 (see Table I) and consistent with the GLCs inferred from experimental data [10]:

$$\text{GLC}_H = p_{hs}\,\tau_{BW}\,H(T_{hs}) > 1, \tag{1}$$

$$\text{GLC}_L = \frac{p_{hs}}{420\ \text{Gbar}}\frac{r_{hs}}{50\ \mu\text{m}} > 1. \tag{2}$$

Here p_{hs} is the hot-spot pressure, τ_{BW} is the burn duration, $H(T_{HS})$ is a function of temperature [42] that accounts for x-ray loss due to the presence of ablator mixing into the hot spot, and r_{hs} is the radius of the hot spot. These values are directly extracted from the simulations and inferred from the experimental data. The burn duration is directly measured using a gamma reaction history (GRH) diagnostic [56], and the radius and volume of the hot spot are determined from three-dimensional imaging of the primary 14 MeV neutrons [57]. The ion temperature is measured from Doppler broadening of the D-T and D-D neutron spectrum using neutron-time-of-flight (NTOF) detectors [58]. The density of the hot spot is inferred from the fusion energy produced, the known D-T and D-D temperature-dependent reaction rates, the measured burn duration, and the measured hot spot volume. The inferred measured pressure is then a function of the inferred density and measured temperature of the hot spot. This method has been validated against a database of ensemble simulations spanning the performance and input parameter space of N210808 [59]. N210808, however, did not reach the National Academy of Sciences definition of ignition of target gain, $G_{target} > 1$ (fusion energy out exceeds the amount of laser energy imparted to the hohlraum), due to the inefficiencies of converting laser light to x-ray radiation drive.

Follow-on experiments to test the variability in performance given the current NIF system capability produced $>$ 50% of the neutron yield of N210808 (experiment N211107), currently the second highest performing experiment on NIF with a capsule gain of > 3. A major limiting factor in reproducing the performance of N210808 has been obtaining capsules of the same quality (number of defects that can seed hydrodynamic instabilities and size of DT fill tube) compared to N210808 which can increase mixing into the hot spot and reduce hot-spot temperature. Another issue has been an unintentional odd mode asymmetry which reduces coupling of fuel KE to hot-spot internal energy. These issues were verified through experimental measurements and agree with the expected reduction in performance given the level of observed perturbation. Work to identify the source of the imperfections and improve the capsule quality to the level of N210808 is ongoing as well as work to improve robustness of the design to these target imperfections.

In summary, N210808 was the first experiment [9] to reach Lawson's criterion for ignition in the laboratory [10] which made intentional design changes compared to predecessor experiments. This proof-of-principle experiment demonstrates that there is nothing fundamentally limiting fusion ignition in the laboratory. N210808, a Hybrid-E experiment, builds on the previous burning plasma Hybrid-E design by further optimizing the coast time through improving the hohlraum efficiency. In addition target fabrication quality enabled realizing the full design potential, and N210808 is a culmination of the effort to increase implosion scale on the NIF to couple more energy to the hot spot while maintaining high hot-spot pressures, without having additional laser energy available to drive the implosion compared to smaller scale experiments. This was achieved by the use of CBET in low-gas-filled hohlraums and using a semianalytical model and detailed radiation hydrodynamics modeling to optimize the hohlraum design. Various optimizations to improve overall performance were performed using radiation hydrodynamics simulations of the integrated hohlraum and capsule assembly. Future work will study the input conditions of N210808, variability to fielding these experiments and modifications to further increase the ρR of the compressed shell and hot spot for increased confinement time which will improve fuel burn-up fraction. Increasing the energy coupled to the hot spot through future improvements in hohlraum efficiency and the use of more laser driver energy are also being considered to drive thicker ablators and DT ice layers, which would improve hydrodynamic stability.

ACKNOWLEDGMENTS

This work was performed under the auspices of U.S. Department of Energy by Lawrence Livermore National Laboratory under Contract No. DE-AC52-07NA27344. This document was prepared as an account of work sponsored by an agency of the United States government. Neither the United States government nor Lawrence Livermore National Security, LLC, nor any of their employees makes any warranty, expressed or implied, or assumes any legal liability or responsibility for the accuracy, completeness, or usefulness of any information, apparatus, product, or process disclosed, or represents that its use would not infringe privately owned rights. Reference herein to any specific commercial product, process, or service by trade name, trademark, manufacturer, or otherwise does not necessarily constitute or imply its endorsement, recommendation, or favoring by the United States government or Lawrence Livermore National Security, LLC. The views and opinions of authors expressed herein do not necessarily state or reflect those of the United States government or Lawrence Livermore National Security, LLC, and shall not be used for advertising or product endorsement purposes. Author contributions: A.L.K. lead designer for Hybrid-E and N210808, integrated hohlraum team lead, asymmetry physics, designer for hohlraum scans, strategy for parameter optimization, wrote this paper; A.B.Z. hot-spot and igni-

tion metrics lead, Hybrid-E experimental lead, N210808 shot responsible individual (RI), strategy for parameter optimization; D.A.C. Hybrid hohlraum strategy, hohlraum LEH scans concept, and semiempirical hohlraum asymmetry model; O.A.H. Hybrid capsule physics strategy, theory, coast-time and asymmetry physics; C.R.W. capsule/instability physics; D.S.C. capsule/instability physics; C.V.Y. integrated capsule-hohlraum simulations; J.E.R. LEH experiments and Hybrid-E shot RI (N210207); D.T.C. Hybrid-E shot RI, Hybrid-B experimental lead, asymmetry physics working group (WG) lead; A.P. x-ray mix analysis and experimental team lead for stagnation; O.L.L. hohlraum window redesign, physics-facility integration group (PFIG) lead, program management; B.B. penumbral x-ray diagnostic; K.L.B. Hybrid-E Shot RI (N210307); L.B.H. Lead designer for HDC campaign; S.D.B. cryo layering; J.B. HDC (diamond) capsule material science and development; R.M.B. real-time nuclear activation diagnostic (RTNAD); N.W.B. Neutron Imaging System (NIS) diagnostic; T.B. capsule fabrication and metrology; T.M.B. cryo layering; P.M.C. VISAR diagnostic; H.C. GLEH x-ray diagnostic; C.C. target fabrication planning; L.D. hot-spot analysis; T.D. LEH experiments Shot RI; D.F. NIS diagnostic; M.J.E. program management; M.G.J. MRS diagnostic; N.G. solid radiochemistry diagnostic; S.H. iPOM analysis; K.D.H. nuclear activation diagnostic; E.H. neutron time-of-flight (NTOF) diagnostics; D.E.H. hohlraum physics, CBET studies in Hybrid-C; D.D.H. Designer for HDC campaign; M.H. Hybrid-E and LEH experiments Shot RI; J.P.H. x-ray diagnostics; H.H. HDC capsule fabrication; N.I. x-ray diagnostics; J.J. NTOF diagnostics; O.J. hohlraum physics; S.M.K. NTOF diagnostics; S.F.K. SPIDER diagnostic; H.G.K. GRH diagnostic; V.G.K. NIS diagnostic; C.K. HDC capsule fabrication; K.M.L. NIS diagnostic; S.L.P. Hybrid-E Shot RI, HDC campaign; N.C.L. optical diagnostics; J.D.L. hot-spot models and ignition metrics; B.J.M. asymmetry assessment, PFIG, laser performance assessment; A.J.M. diagnostic management; A.G.M. x-ray diagnostics; E.V.M. x-ray diagnostics; K.M. GRH diagnostic; M.M. VISAR diagnostic; A.S.M. nuclear diagnostics; K.N. project engineering; J.G.D.N. MOR and PAM stability, SSD improvements, and FC control; A.N. target fabrication engineering, capsule, and fabrication planning; R.N. ensemble simulations; P.K.P. hot-spot models and ignition metrics; N.G.R. capsule fabrication; M.S.R. DANTE diagnostic; J.S. mode-1 capsule analysis, cryo layering; D.J.S. NTOF diagnostics; S.M.S. HYDRA code development; K.S. mode-1 metrology; S.J.S. sagometer data and particle analysis; M.S. target fabrication lead; S.S. x-ray diagnostics; D.J.S. hohlraum/LPI physics; C.A.T. Designer for Bigfoot campaign; R.T. x-ray diagnostics, Hybrid-E shot RI; C.T. x-ray diagnostics; E.R.T. optical diagnostics; P.L.V. NIS diagnostic; C.W. HDC capsule coating development and fabrication; D.T.W. hohlraum physics; S.T.Y. MOR and PAM stability, SSD improvements, and FC control.

APPENDIX

1. Simulation methodology

The simulations use a common methodology of applying a common adjustment (artificial multipliers on the input laser power) of the radiation drive to match existing parameter "tuning" data (gas capsule experiments that measure the in-flight symmetry and velocity near implosion peak velocity and shock timing experiments), and then application of the spatially, temporally, and frequency-resolved radiation drive to higher resolution capsule-only simulations to additionally model perturbations such as the capsule support tent and DT fill tube [55,60]. All simulations also use the as-shot laser delivery as well as interface roughness, which varies between experiments.

A fall-line interface mix model for mixing material at the DT fuel-ablator interface [61] was included and set to initiate relative to when the calculated Atwood number became unstable. This model mixes isotopes over a user-defined layer relative to the interface between the two materials being mixed. The amount of mixing is a fraction of the user-defined "fall-line," and the timing for the mix is defined by the user with the additional criteria that the acceleration between the interface of the heavy and light liquids is in the unstable direction. Since N210808 was calculated to always have a stable Atwood number, a fall-line mix model was not used.

Modes one, two, and four of the Legendre decomposition of the radiation drive were included in the simulations. Mode two of the radiation drive flux asymmetry was multiplied by a factor of $\sim$0.7 in the "peak" to match the observed symmetry. The radiation hydrodynamic calculations using HYDRA include detailed equations of state [62,63], transport [64,65], electron-ion coupling [66,67], and opacity models [68]). In this study, the equation-of-state model for the carbon ablator was LEOS table 9067 [69].

2. Laser back-scatter

The measured laser light that was scattered back out of the hohlraum as a result of laser plasma interactions was similar to the previous burning plasma Hybrid-E platform (N210207) and $>30\times$ less backscatter than previous high-gas-filled hohlraums (e.g., N140520). The stimulated Brillouin scattering (SBS) on the "inner" (23° and 30°) cones for these three experiments was $\sim$0–1 kJ per cone, with large error bars (up to 16 kJ) backscattered from the "inner" 23° cone for N210808. The stimulated Raman scattering for N210808 (2.8 ± 1.1 kJ) and N210207 (0.74 ± 0.28 kJ) were significantly less than for N140520 (81 ± 32 kJ per cone and $\sim$162 kJ total for the "inner" beams), which was also fielded with $\sim$150 kJ less laser energy incident on target. Differences between N210808 and N210207, although small, could be attributed to the change in wavelength separation required to regain symmetry for the N210808 platform. The SBS on the "outer" 50° beams was reduced for N210808 (4.8 ± 2.4 kJ) compared to N210207 (9.5 ± 3.4 kJ) as a result of more energy being transferred from the "outer" beams to the "inner" beams. The 44.5° SBS was similar to the 50° beam SBS for N210207 and N210808. Both N210207 and N210808 showed less "outer" beam SBS than N140520, which was 13 ± 5.2 kJ on the 44.5° beams and 33 ± 6.6 kJ on the 50° beams. The "outer" SRS was < 1 kJ for N210207 and N210808 and 3.4 ± 0.70 kJ for N140520. In total N140520 (1.76 MJ incident laser energy) backscattered $\sim$216 kJ of laser light out of the hohlraum compared to $\sim$15.5 kJ for N210207 (1.930 MJ incident laser energy) and $\sim$13.4 kJ for N210808 (1.92 MJ incident laser energy).

[1] J. Nuckolls, L. Wood, A. Thiessen, and G. Zimmerman, Nature (London) **239**, 139 (1972).

[2] J. S. Clarke, H. N. Fisher, and R. J. Mason, Phys. Rev. Lett. **30**, 249 (1973).

[3] R. F. Post, Rev. Mod. Phys. **28**, 338 (1956).

[4] G. S. Fraley, E. J. Linnebur, R. J. Mason, and R. L. Morse, Phys. Fluids **17**, 474 (1974).

[5] J. D. Lawson, Proc. Phys. Soc. B **70**, 6 (1957).

[6] A. L. Kritcher, J. Ralph, D. E. Hinkel, T. Doppner, M. Millot, D. Mariscal, R. Benedetti, D. J. Strozzi, T. Chapman, C. Goyon *et al.*, Phys. Rev. E **98**, 053206 (2018).

[7] A. L. Kritcher, A. B. Zylstra, D. A. Callahan, O. A. Hurricane, C. Weber, J. Ralph, D. T. Casey, A. Pak, K. Baker, B. Bachmann *et al.*, Phys. Plasmas **28**, 072706 (2021).

[8] E. I. Moses *et al.*, J. Phys.: Conf. Ser. **688**, 012073 (2016).

[9] A. B. Zylstra, A. L. Kritcher, O. A. Hurricane, D. A. Callahan, J. E. Ralph, D. T. Casey, A. Pak, O. L. Landen, B. Bachmann, K. L. Baker *et al.*, Phys. Rev. E **106**, 025202 (2022).

[10] H. Abu-Shawareb *et al.* (Indirect Drive ICF Collaboration), Phys. Rev. Lett. **129**, 075001 (2022).

[11] J. Lindl, Phys. Plasmas **2**, 3933 (1995).

[12] J. D. Lindl, P. Amendt, R. L. Berger, S. G. Glendinning, S. H. Glenzer, S. W. Haan, R. L. Kauman, O. L. Landen, and L. J. Suter, Phys. Plasmas **11**, 339 (2004).

[13] S. W. Haan, J. D. Lindl, D. A. Callahan, D. S. Clark, J. D. Salmonson, B. A. Hammel, L. J. Atherton, R. C. Cook, M. J. Edwards, S. H. Glenzer *et al.*, Phys. Plasmas **18**, 051001 (2011).

[14] A. L. Kritcher, R. Town, D. Bradley, D. Clark, B. Spears, O. Jones, S. Haan, P. T. Springer, J. Lindl, R. H. H. Scott *et al.*, Phys. Plasmas **21**, 042708 (2014).

[15] O. A. Hurricane, D. T. Casey, O. Landen, A. L. Kritcher, R. Nora, P. K. Patel, J. A. Ganey, K. D. Humbird, J. E. Field, M. K. G. Kruse, J. L. Peterson, and B. K. Spears, Phys. Plasmas **27**, 062704 (2020).

[16] B. J. MacGowan, O. Landen, D. Casey, C. Young, D. Callahan, E. Hartouni, R. Hatarik, M. Hohenberger, T. Ma, D. Mariscal *et al.*, High Energy Density Phys. **40**, 100944 (2021).

[17] D. T. Casey, B. J. MacGowan, J. D. Sater, A. B. Zylstra, O. L. Landen, J. Milovich, O. A. Hurricane, A. L. Kritcher, M. Hohenberger, K. Baker *et al.*, Phys. Rev. Lett. **126**, 025002 (2021).

[18] T. R. Dittrich, O. A. Hurricane, D. A. Callahan, E. L. Dewald, T. Doppner, D. E. Hinkel, L. F. B. Hopkins, S. Le Pape, T. Ma, J. L. Milovich *et al.*, Phys. Rev. Lett. **112**, 055002 (2014).

[19] T. Ma, P. K. Patel, N. Izumi, P. T. Springer, M. H. Key, L. J. Atherton, L. R. Benedetti, D. K. Bradley, D. A. Callahan, P. M. Celliers *et al.*, Phys. Rev. Lett. **111**, 085004 (2013).

[20] A. B. Zylstra, D. T. Casey, A. Kritcher, L. Pickworth, B. Bachmann, K. Baker, J. Biener, T. Braun, D. Clark, V. Geppert-Kleinrath *et al.*, Phys. Plasmas **27**, 092709 (2020).

[21] A. Pak, L. Divol, C. R. Weber, L. F. Berzac Hopkins, D. S. Clark, E. L. Dewald, D. N. Fittinghoff, H. Geppert Kleinrath, M. Hohenberger, S. LePape *et al.*, Phys. Rev. Lett. **124**, 145001 (2020).

[22] D. T. Casey, C. Thomas, K. L. Baker, B. K. Spears, M. Hohenberger, S. F. Khan, R. C. Nora, C. R. Weber, D. T. Woods, O. Hurricane *et al.*, Phys. Plasmas **25**, 056308 (2018).

[23] S. R. Nagel, S. W. Haan, J. R. Rygg, M. Barrios, L. R. Benedetti, D. K. Bradley, J. E. Field, B. A. Hammel, N. Izumi, O. S. Jones *et al.*, Phys. Plasmas **22**, 022704 (2015).

[24] S. Le Pape, L. F. B. Hopkins, L. Divol, N. Meezan, D. Turnbull, A. J. Mackinnon, D. Ho, J. S. Ross, S. Khan, A. Pak *et al.*, Phys. Plasmas **23**, 056311 (2016).

[25] L. F. Berzak Hopkins, N. B. Meezan, S. Le Pape, L. Divol, A. J. Mackinnon, D. D. Ho, M. Hohenberger, O. S. Jones, G. Kyrala, J. L. Milovich *et al.*, Phys. Rev. Lett. **114**, 175001 (2015).

[26] L. Divol, A. Pak, L. F. B. Hopkins, S. L. Pape, N. B. Meezan, E. L. Dewald, D. D.-M. Ho, S. F. Khan, A. J. Mackinnon, J. S. Ross *et al.*, Phys. Plasmas **24**, 056309 (2017).

[27] S. Le Pape, L. F. Berzak Hopkins, L. Divol, A. Pak, E. L. Dewald, S. Bhandarkar, L. R. Bennedetti, T. Bunn, J. Biener, J. Crippen *et al.*, Phys. Rev. Lett. **120**, 245003 (2018).

[28] L. B. Hopkins, S. LePape, L. Divol, A. Pak, E. Dewald, D. D. Ho, N. Meezan, S. Bhandarkar, L. R. Benedett, T. Bunn *et al.*, Plasma Phys. Controlled Fusion **61**, 014023 (2019).

[29] K. L. Baker, C. A. Thomas, D. T. Casey, M. Hohenberger, S. Khan, B. K. Spears, O. L. Landen, R. Nora, D. T. Woods, J. L. Milovich *et al.*, Phys. Rev. E **102**, 023210 (2020).

[30] M. Hohenberger, D. T. Casey, A. L. Kritcher, A. Pak, A. B. Zylstra, C. A. Thomas, K. L. Baker, S. Le Pape, B. Bachmann, R. L. Berger *et al.*, Phys. Plasmas **27**, 112704 (2020).

[31] A. B. Zylstra, A. Kritcher, A. L. Kritcher, O. A. Hurricane, D. A. Callahan, K. Baker, T. Braun, D. T. Casey, D. Clark, K. Clark *et al.*, Phys. Rev. Lett. **126**, 025001 (2021).

[32] A. Kritcher, C. Young, H. Robey, C. Weber, A. Zylstra, O. Hurricane, D. Callahan, J. Ralph, J. Ross, K. Baker *et al.*, Nat. Phys. **18**, 251 (2022).

[33] O. A. Hurricane, D. A. Callahan, P. T. Springer, M. J. Edwards, P. Patel, K. Baker, D. T. Casey, L. Divol, T. Dppner, D. E. Hinkel *et al.*, Plasma Phys. Control. Fusion **61**, 014033 (2019).

[34] O. A. Hurricane, P. T. Springer, P. K. Patel, D. A. Callahan, K. Baker, D. T. Casey, L. Divol, T. DŁoppner, D. E. Hinkel, M. Hohenberger *et al.*, Phys. Plasmas **26**, 052704 (2019).

[35] O. A. Hurricane, A. Kritcher, D. A. Callahan, O. Landen, P. K. Patel, P. T. Springer, D. T. Casey, E. L. Dewald, T. R. Dittrich, T. Doppner *et al.*, Phys. Plasmas **24**, 092706 (2017).

[36] NYYMMDD: YY = year, MM = month, DD = day.

[37] P. K. Patel, P. T. Springer, C. R. Weber, L. C. Jarrott, O. A. Hurricane, B. Bachmann, K. L. Baker, L. F. B. Hopkins, D. A. Callahan, D. Casey *et al.*, Phys. Plasmas **27**, 050901 (2020).

[38] D. A. Callahan, O. A. Hurricane, J. E. Ralph, C. A. Thomas, K. L. Baker, L. R. Benedetti, L. F. Berzak Hopkins, D. T. Casey, T. Chapman, C. E. Czajka *et al.*, Phys. Plasmas **25**, 056305 (2018).

[39] A. Zylstra, O. Hurricane, D. Callahan, A. Kritcher, J. Ralph, H. F. Robey, J. S. Ross, C. V. Young, K. Baker, D. T. Casey *et al.*, Nature (London) **601**, 542 (2022).

[40] J. S. Ross, J. E. Ralph, A. B. Zylstra, A. Kritcher *et al.*, arXiv:2111.04640.

[41] J. D. Lindl, S. W. Haan, O. L. Landen, A. R. Christopherson, and R. Betti, Phys. Plasmas **25**, 122704 (2018).

[42] O. A. Hurricane, S. A. Maclaren, M. D. Rosen, J. H. Hammer, P. T. Springer, and R. Betti, Phys. Plasmas **28**, 022704 (2021).

[43] J. E. Ralph *et al.*, in 63rd Annual Meeting of the American Physical Society Division of Plasma Physics, Vol. 66, no. 13, abstract GO04.00003, Pittsburgh, Pennsylvania, November 8–12, 2021 (unpublished).

[44] J. E. Ralph, T. Woods, A. Kritcher *et al.* (unpublished).
[45] O. A. Hurricane, D. T. Casey, O. Landen, D. A. Callahan, R. Bionta, S. Haan, A. Kritcher, R. Nora, P. Patel, P. Springer *et al.*, Phys. Plasmas **29**, 012703 (2022).
[46] A. Zylstra, O. Hurricane, D. Callahan, A. Kritcher, O. Landen, J. Lindl, A. Pak, P. Patel, J. Ralph, S. Ross *et al.*, Nucl. Fusion **61**, 116066 (2021).
[47] M. M. Marinak, G. D. Kerbel, N. A. Gentile, O. Jones, D. Munro, S. P. and T. R. Dittrich, and S. W. Haan, Phys. Plasmas **8**, 2275 (2001).
[48] P. Michel, L. Divol, E. A. Williams, S. Weber, C. A. Thomas, D. A. Callahan, S. W. Haan, J. D. Salmonson, S. Dixit, D. E. Hinkel *et al.*, Phys. Rev. Lett. **102**, 025004 (2009).
[49] J. D. Moody, P. Michel, L. Divol, R. L. Berger, E. Bond, D. K. Bradley, D. A. Callahan, E. L. Dewald, S. Dixit, M. J. Edwards *et al.*, Nat. Phys. **8**, 344 (2012).
[50] L. A. Pickworth, T. Dppner, D. E. Hinkel, J. E. Ralph, B. Bachmann, L. P. Masse, L. Divol, L. R. Benedetti, P. M. Celliers, H. Chen *et al.*, Phys. Plasmas **27**, 102702 (2020).
[51] S. J. Ali, P. M. Celliers, S. Haan, T. R. Boehly, N. Whiting, S. H. Baxamusa, H. Reynolds, M. A. Johnson, J. D. Hughes, B. Watson *et al.*, Phys. Plasmas **25**, 092708 (2018).
[52] C. R. Weber, D. S. Clark, A. Pak, N. Alfonso, B. Bachmann, L. F. B. Hopkins, T. Bunn, J. Crippen, L. Divol, T. Dittrich *et al.*, Phys. Plasmas **27**, 032703 (2020).
[53] A. L. Kritcher, D. T. Casey, C. A. Thomas, A. B. Zylstra, M. Hohenberger, K. Baker, S. Le Pape, B. Bachmann, S. Bhandarkar, J. Biener *et al.*, Phys. Plasmas **27**, 052710 (2020).
[54] D. S. Clark, S. W. Haan, A. W. Cook, M. J. Edwards, B. A. Hammel, J. M. Koning, and M. M. Marinak, Phys. Plasmas **18**, 082701 (2011).
[55] D. S. Clark, C. R. Weber, J. L. Milovich, A. E. Pak, D. T. Casey, B. A. Hammel, D. D. Ho, O. S. Jones, J. M. Koning, A. L. Kritcher *et al.*, Phys. Plasmas **26**, 050601 (2019).
[56] H. W. Herrmann, N. Homan, D. C. Wilson, W. Stoe, L. Dauy, Y. H. Kim, A. McEvoy, C. S. Young, J. M. Mack, C. J. Horseld *et al.*, Rev. Sci. Instrum. **81**, 10D333 (2010).
[57] P. Volegov *et al.*, Rev. Sci. Instrum. **85**, 023508 (2014).
[58] V. Y. Glebov, T. C. Sangster, C. Stoeckl, J. P. Knauer, W. Theobald, K. L. Marshall, M. J. Shoup, T. Buczek, M. Cruz, T. Duy *et al.*, Rev. Sci. Instrum. **81**, 10D325 (2010).
[59] A. Zylstra, R. Nora, P. Patel, and O. Hurricane, Phys. Plasmas **28**, 122703 (2021).
[60] D. S. Clark, C. Weber *et al.*, Phys. Plasmas **23**, 056302 (2016).
[61] L. Welser-Sherrill, J. Cooley, D. Haynes, D. Wilson, M. Sherrill, R. Mancini, and R. Tommasini, Phys. Plasmas **15**, 072702 (2008).
[62] L. X. Benedict, K. P. Driver, S. Hamel, B. Militzer, T. Qi, A. A. Correa, A. Saul, and E. Schwegler, Phys. Rev. B **89**, 224109 (2014).
[63] J. Gaffney, S. Hu, P. Arnault, A. Becker, L. Benedict, T. Boehly, P. Celliers, D. Ceperley, O. Certik, J. Clerouin *et al.*, High Energy Density Phys. **28**, 7 (2018).
[64] M. P. Desjarlais, C. R. Scullard, L. X. Benedict, H. D. Whitley, and R. Redmer, Phys. Rev. E **95**, 033203 (2017).
[65] L. G. Stanton and M. S. Murillo, Phys. Rev. E **93**, 043203 (2016).
[66] Y. Lee and R. More, Phys. Fluids **27**, 1273 (1984).
[67] C. R. Scullard, S. Serna, L. X. Benedict, C. L. Ellison, and F. R. Graziani, Phys. Rev. E **97**, 013205 (2018).
[68] C. A. Iglesias and F. J. Rogers, Astrophys. J. **464**, 943 (1996).
[69] A. Correa, L. Benedict, D. Young, E. Schwegler, and S. A. Bonev, Phys. Rev. B **78**, 024101 (2008).